To appear in: Iranian Journal of Earth Sciences (Iran J. Earth. Sci.)

E-ISSN: 2228-785X Print ISSN: 2008-8779

Received: 14 January 2024 Revised: 4 October 2024

Accepted: 18 April 2025

DOI: https://doi.org/10.57647/j.ijes.2025.16942

Original Research

ASTER Spectral Analysis and Lithologic Mapping of Qa'le Hasan Ali Quaternary Volcano in Central Iran

Maliheh Ghoorchi[1]*, Saeed Saadat[1]

1.Department of Petroleum Engineering and Geology, Ma.C., Islamic Azad University, Mashhad, Iran

**Corresponding author: Maliheh.Ghoorchi@iau.ac.ir*

Abstract

This study focuses on results derived from satellite image processing of the Qa'le Hasan Ali Quaternary crater, located in Central Iran, utilizing ASTER data. Band Ratio, Spectral Angle Mapper, Principal Component Analysis, Minimum Noise Fraction, Support Vector Machine and Random Forest techniques were used for mapping various rocks, and minerals in this area. The color composites from the band ratios (B5, B6, and B8), the PCA transform technique on bands 1, 2, 5, and 8 and 1, 3, 4, and 6 (visible, NIR and SWIR) of ASTER data show distribution of different rocks

and minerals. The SAM result displays an acceptable matching with mirabilite, gypsum, calcite, dolomite, aragonite minerals, and epidote and chlorite as well. The RF and SVM algorithms show an improvement in the classification of related lithology in the study area. The lithologies enhanced by ASTER data showed excellent match with field evidence, petrographic studies, and the available geologic map. The distribution haloes of the volcanic craters are aligned with field observations. The confuse matrix and the overall accuracy yield 89.15% for SVM compared to 84.41% accuracy for RF classification. Previous geochemical and isotopic published data indicate this Quaternary volcano contains xenoliths with carbonatite affinities and potential for rare earth elements. Further studies are recommended to explore the potential for REE deposit in the area and to expand the application of these methods to other volcanic craters in the region.

Keywords: *ASTER, late Quaternary volcano, REE, Qa'le Hasan Ali crater, central Iran.*

1. Introduction

Remote sensing data have been utilized in many scientific fields for producing thematic maps to display rock type, hydrothermal alteration, and mineral mapping. Based on a literature review by Ramsey and Flynn (2020), over the course of 24 years (1995 to 2019), more than 270 papers were published related to volcanology using ASTER data out of which less than 20 percent of them focused specifically on mapping. These papers commonly describe how the future ASTER data could be utilized for volcanic studies. However, very few researchers applied satellite-based enhanced data to volcanic activities related to carbonatite occurrences, which can play a role as the source for rare earth elements (REEs).

Mapping geological outcrops is an essential part of mineral exploration, mining and ore extraction. Carbonatites are the main source of REEs, comprising predominantly of carbonate minerals (more than 50 modal% carbonate minerals). These rocks are generally confined to alkaline magmatism controlled by rift-related settings. Mineralization tends to be associated with the silica-oversaturated, where silica-under saturated magmas can host REEs, P, U, Th, and F elements (Pirajno 2015). Rajendran and Nasir (2013) have utilized the ASTER data to differentiate these rocks in TIR and VNIR-SWIR region, based on absorption characters of carbonate minerals. Libeesh et al. (2022) integrated BR and PCA to lithological mapping of Ultramafic–Alkaline–complex (India). Machine learning algorithms including support vector machine (SVM) and random forests (RF) have been applied to remote sensing image classifications (Ghasempour et al. 2014; Masoumi et al. 2017; Yazdi et al. 2019; Nazari et al. 2023; Bahrami et al. 2024; Mohammadi et al. 2020; Abdolahadi et al. 2025).

Quaternary magmatic activities have been reported from Qa'le Hasan Ali (QHA) and Bazman and Taftan in southeast Iran, as well as in Pakistan and Afghanistan (Fig. 1). Bazman, Taftan, and Kuh-e-sultan volcanos are related to the convergent plate Makran volcanic arc setting, while the QHA and Khanneshin (Afghanistan) occur at the extreme western and eastern, respectively, extension of this arc and may be related to rift setting (Mars and Rowan 2011; Saadat and Stern 2011; Dabiri et al. 2019; Mollai et al. 2021; Ousta et al. 2024; Salehpour et al. 2025). Based on the studies of Saadat and Stern (2011), Sabzehei (1984) and Shishebore (1993); the tectonics of the study area indicates an intracontinental rift environment for the Quaternary volcanoes associated with craters, and it is not related to subduction.

The main purpose of this study is to evaluate ASTER data for mapping late Quaternary QHA maars, which contain xenoliths with carbonatite affinities and have potential for rare earth elements (REEs) in central Iran. This effort is to contribute toward opening a window for further studies in this potentially valuable locality located around 700 kilometer west of Khanneshin carbonatite volcano of Afghanistan (Fig. 1).

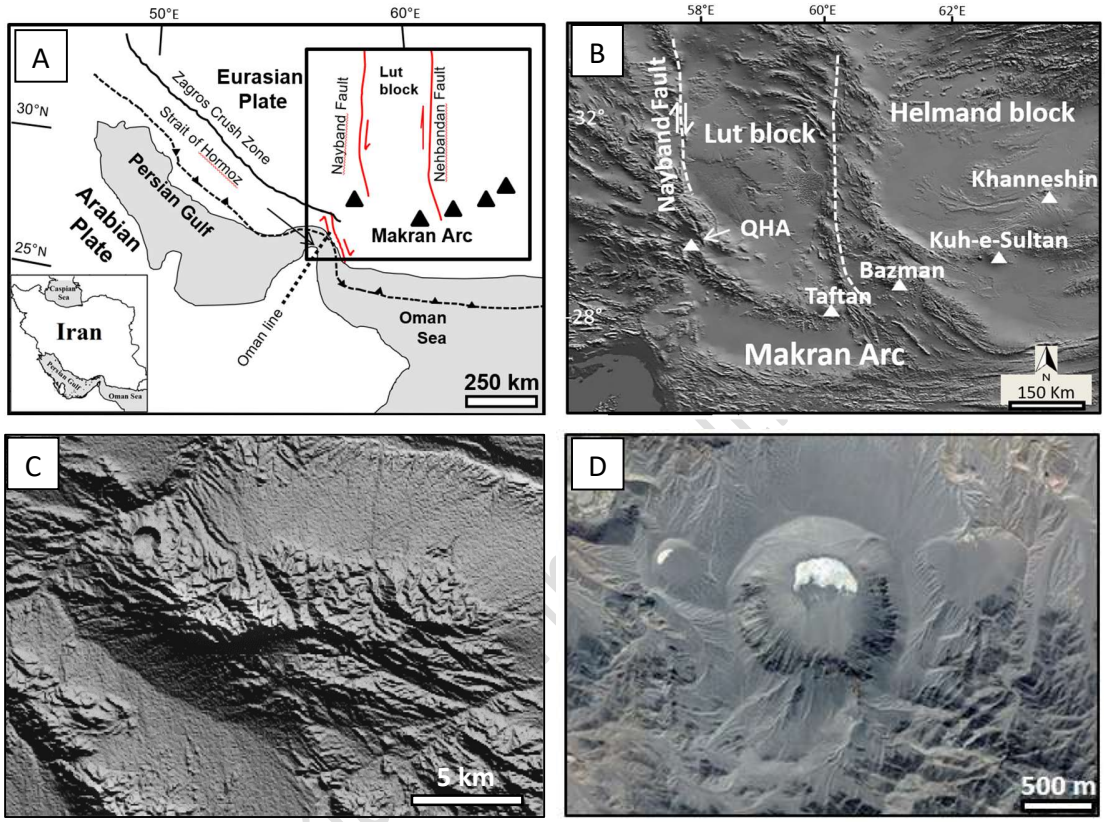

Fig. 1. (A) General tectonic setting of the southern part of eastern Iran demonstrating major faults (red lines) in Eastern Iran, Lut block, and the Quaternary volcanos from south eastern Iran, Pakistan, and Afghanistan (B). The location of these major volcanoes in DEM image (after Saadat and Stern (2011) and references there in). (C) DEM (Digital Elevation Model), showing the topographic framework of the study area. (D) A view of the crater from QHA maars in Google Earth image.

2. Geological setting

The study area is located in central Iran, at the intersection of the Nayband fault (north-south trend) with other faults trending northwest–southeast (Fig. 1). The QHA includes 14 maars that intrude Eocene magmatic rocks of the Urumieh–Dokhtar belt. The diameter of these post-collisional maars varies from 120 to more than 1000 meters with shapes varying from circular to oval. The largest of these maars is 1200 meters wide and around 250 meters depth. The areas around the craters are characterized by crushed zones and hydrothermal alteration. The maars produced tephritic

pyroclastic deposits. Magmatic materials erupted in the last stage of the explosions that formed the craters include volcanic bombs, scoria, lapilli, and volcanic ash. Ar-Ar dating of phlogopite in volcanic bomb samples from the Great Crater yields ages of 112–119 ka (Pang et al. 2015).

The study area was once believed to be meteorite impact craters (Gojkovic´ 1972). Milton (1976) later identified the area as containing highly potassic tephrites associated with late Quaternary maars. Sabzehei (1984) and Shishebore (1993) reported the resemblance of the highly potassic alkaline rocks to either kamafugites and/or the lamproite clan, respectively. Saadat et al. (2014) presented new petrochemical information for QHA maars. Magmatic calcite was observed in the groundmass of some granular extrusive samples and in some cognate xenoliths, suggesting that the highly potassic alkaline rocks have certain affinities with carbonatites.

According to the 1:100,000 geological map (Khaneh Khatun map), the most important geological units are: Andesite, basalt, rhyolite, rhyodacite, pyroclastic, agglomerate, tuff, tuffaceous sandstone, alluvial and gravel fan (Fig. 2). The Eocene volcanic rocks can be subdivided into three fairly clear subcomplexes (Djokovic´ et al. 1972); the lower one consisting mainly of pyroclastics with some tuffaceous sandstones in a few units; the middle one or the Hezar sequence and the upper one with sediment and subordinate volcanic.

The lower subcomplex begins with rhyodacites accompanied by agglomerate, followed by an alternation of rhyolitic, rhyodacitic, and sparse andesitic, trachy basaltic, and andesite-basaltic rocks. The middle subcomplex is composed of andesite-basalt, andesite, basalt, rhyolite, trachy basalt and rhyodacite with pyroclastics showing a characteristic alternation of more basic and more acidic rocks (Djokovic´ et al. 1972). Travertine is visible in some areas of the plains around the heights and the bottom of the valleys. According to the field evidence, volcanism occurred after the deposition of travertine. The concentration of limestone veins is higher in the northeast of the village of QHA. Dikes are often observed with a northwest-southeast trend.

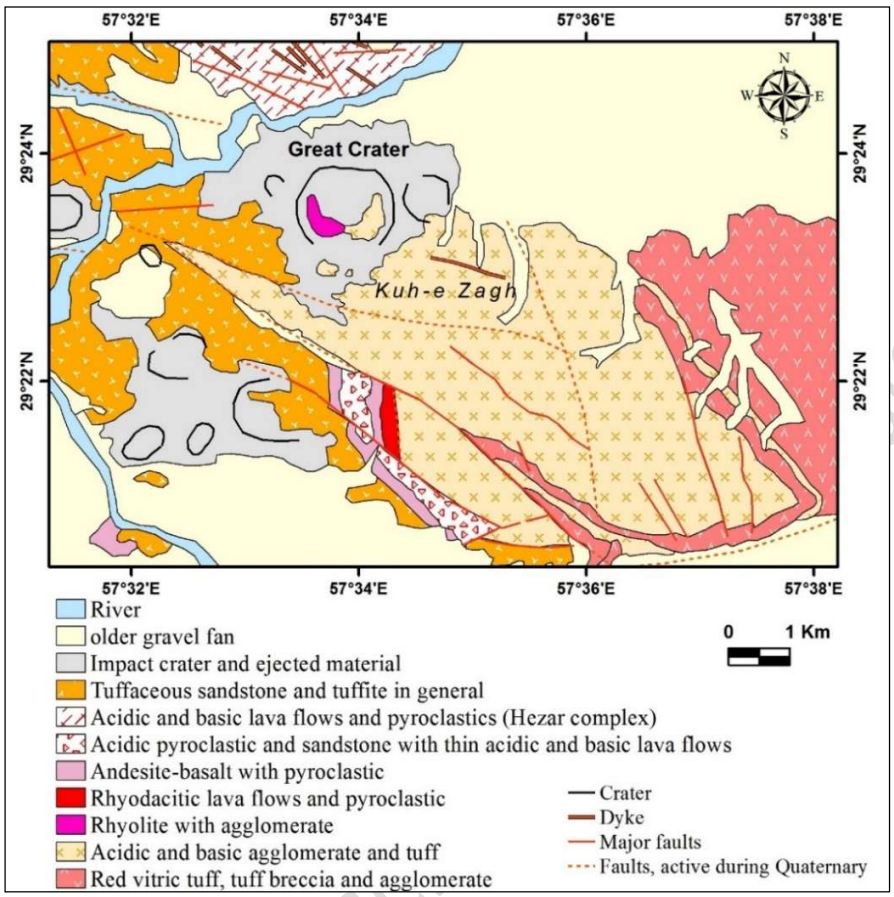

Fig. 2. Geological map of QHA area (After Djokovic´ et al. 1972).

3. Materials and Methods:

3.1. Data acquisition and pre-processing

ASTER was launched on EOS-Terra in 2000. ASTER images provide 14 different wavelengths, ranging from visible (VNIR), shortwave infrared (SWIR) to thermal infrared bands (TIR) (Table 1). This setup helps ASTER sensor to be more appropriate for making distinctions and mapping of rocks and minerals than other sensors such as Landsat. Detection of features in satellite images depends on utilization of proper spectral bands. The VNIR and SWIR wavelengths (0.45 to 2.5 μm) may be applied to better define the composition of minerals (Clark 1999). The VNIR region can be applied for iron oxides and REEs based on the absorption features (Hunt 1977). The multispectral ASTER L1B-level data, acquired 2001-07-01, was utilized. Data processing has been done by ENVI (Environment for Visualizing Images) software. The satellite images were geometrically calibrated. All bands were co-registered into a single file and resampled to a spatial resolution of 15 m. The images were spectrally and spatially subset for processing. The log residual method was utilized to perform atmospheric corrections and converting radiance to reflectance.

Table 1. Sensor Specifications of ASTER (Fujisada, 1995)

Subsystem	Band number	Spectral range (μm)	Spatial resolution (m)	Quantization level (bits)
VNIR	1	0.52–0.60	15	8
	2	0.63–0.69		
	3N	0.78–0.86		
	3B	0.78–0.86		
SWIR	4	1.600–1.700	30	8
	5	2.145–2.185		
	6	2.185–2.225		
	7	2.235–2.285		
	8	2.295–2.365		
	9	2.360–2.430		
TIR	10	8.125–8.475	90	12
	11	8.475–8.825		
	12	8.925–9.275		
	13	10.25-10.95		
	14	10.95-11.65		

3.2. Processing data

In this study, different algorithms were applied on ASTER data, including Band ratios (BR), Spectral Angel Mapper (SAM), Principal Component Analysis (PCA), Selective principal components analysis (SPCA), and two machine learning algorithms: Random Forest (RF) and Support Vector Machine (SVM).

A band ratio is created by the division of two sets of band digital numbers for each pixel. It is a simple and powerful method generally utilized for geological studies (Abrams et al. 1983; Abrams 2000). SAM is a supervised classification algorithm which identifies the various classes in the image based on the calculation of the spectral angle. The classification chooses the library spectrum that has the smallest spectral angle with each pixel in the input image. SAM classification categorizes images with respect to "endmembers" (Kruse et al. 1993; Boardman and Kruse 1994; Dennison et al. 2004; Mundt et al. 2007). Appropriate classification thresholds are one of the most important factors. Hadigheh and Ranjbar (2013) used SAM and Spectral Information Divergence (SID) for geological mapping.

PCA is a linear dimensionality reduction technique and an unsupervised learning algorithm. The PCA used to examine the interrelations among a set of variables and allows for compressing highly correlated bands into one single band. This method can eliminate radiation effects to better detect any geological phenomena (Crosta et al. 2003).

Machine learning techniques have demonstrated considerable potential in improving the efficiency and accuracy of lithological classification (Farhadi et al., 2024). SVM is a powerful supervised algorithm with a simple structure that is utilized in several studies because of its advantages in improved convergence, optimal solution and generalization ability to solve problems with high-dimensionality (Pal and Mather 2005). SVM classifies data by finding the best hyperplane that has

the maximum distance between data. Farhadi et al (2022) used combination of SVM with fractal method for soil geochemical anomaly detection in sediment-hosted Pb-Zn Deposit, Central Iran. Rahmani et al. (2025) applied the SVM algorithm on PRISMA data for lithological mapping.
The RF algorithm, a supervised classification method, is an extension of the decision tree approach (Breiman 2017). RF classification can be interrogated to examine which of the input features have the more impactful upon the final classification. Technical flowchart of the methodology is shown in Figure 3.

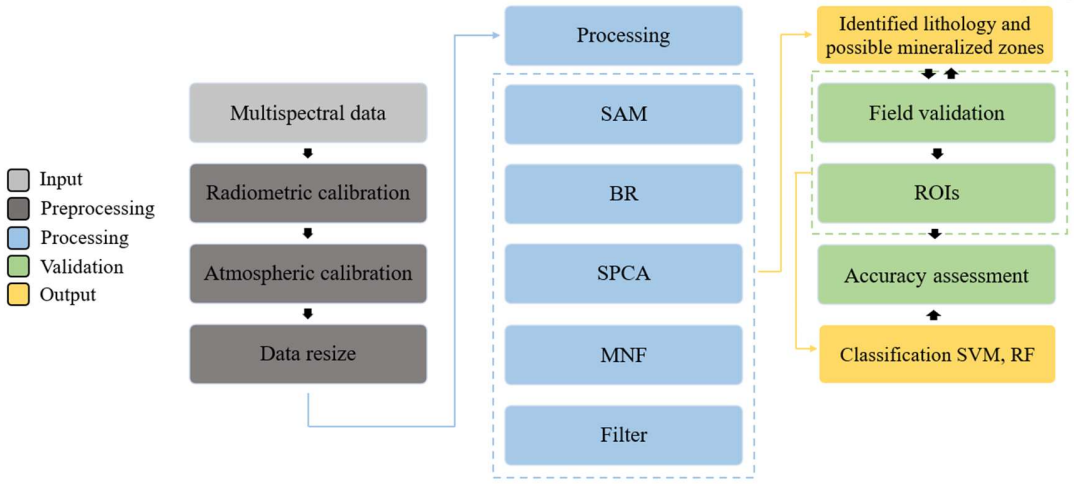

Fig. 3. Technical flowchart of the image processing methodology in this research; (ROIs, training pixels by Regions of Interest).

Some surface spectra are used from the USGS (U.S. Geological Survey), JPL (NASA Jet Propulsion Laboratory) and JHU (Johns Hopkins University) spectral library (Fig. 4). By resampling the spectra data from these typical spectral libraries, the spectral datasets with different spectral resolutions can be obtained for the hyperspectral or multispectral remote sensing (Fig. 4B). Carbonate minerals show noticeable spectral absorption in the SWIR within the wavelength ranging between 2.50–2.55 µm and 2.30–2.35 µm (van der Meer 1995, Gupta 2003) (Fig. 4). Positions of the carbonate bands are indicative of mineralogy (Gaffey 1986). The absorption feature of calcite displays strong absorption near 2.335 and 2.528 µm, where dolomite and siderite display strong adsorption after 2.3 and 2.5 µm. Calcite exhibit weak absorption near 1.875, 1.995, and 2.155 µm (Fig. 4). The amount of Mg, Fe and Mn replacing Ca in carbonates can change the location and shape of indicative absorption features in the SWIR bands (Laukamp et al. 2021).

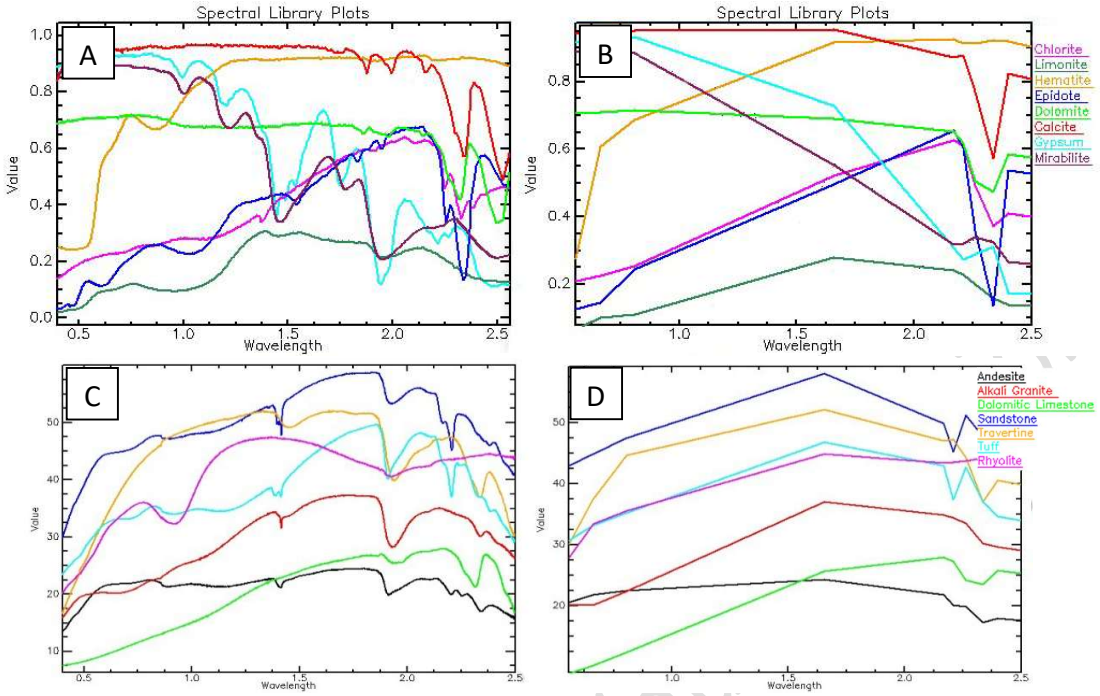

Fig. 4. Spectral features of some minerals (calcite, dolomite, epidote, gypsum, chlorite, limonite, hematite and mirabilite) and rocks (basaltic andesite, alkali granite, rhyolite, and sandstone), A, Data from the USGS spectral library C) Data from the JHU spectral library, B, D) Data resampled according to ASTER bands.

Structural patterns are important in mineralization. For example, Nabilou et al. (2022), based on the fractal modelling results in Gazestan deposit (Iran), proposed the high REE concentrations occurred close to the main fault. The QHA area is a tectonized and fractured area. It seems strike-slip faults play essential role in replacement of Quaternary magmatism and have facilitated the transfer of ultrapotassic magmatism in the upper crust (Shishebore 1993). Enhancement of structural patterns (faults) was done by various filters. Directional filter (45°, 135°and 225°) associated band combination (e.g., 6, 3 and 1) was chosen for mapping lineaments. The color composite image from SPCA on bands 1, 3, 4 and 6 (RGB: -PC2, PC3, PC4) and directional filter were chosen to identify circular features (Fig. 5). A total of 30 lineaments have been evaluated as potential faults (Fig. 14B). Most of the results are consistent with the general trend of faults introduced in the existing maps at 1:100000 scale. New faults were also highlighted. Minor faults mostly have northwest-southeast and sometimes north-south direction. The density of faults does not correspond to the locations of explosive volcanoes.

The processing results were compared with available field data and geological maps to assess ASTER's ability in geological mapping. Samples were collected from the QHA during field studies to examine the remote sensing method's detection accuracy of different rocks directly.

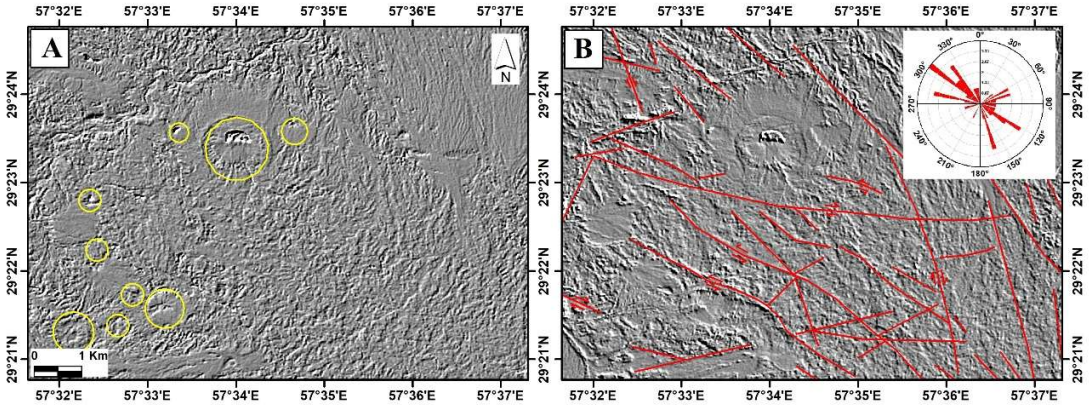

Fig.5. Identification of lineaments (faults) and circular structures using aster images: A) Directional filter at 225°, B) Directional filter at 135°.

4. Results and discussion

Results derived from the BR techniques show proper separation of the boundary of rock units of the study area. A decorrelation stretch removes the highly correlated data between bands to produce more colorful and interpretable images. In this study, a DS technique was applied to the SWIR bands (631) and (468) to separate the QHA crater and ejected area, from other rock units. The extent of the largest crater in the QHA volcanos, the 'Great Crater', and surrounding flows are noticeable in false color composite (FCC) image (RGB: 631) with a circular feature (Fig. 6A). The area of the eruption around the crater can also be distinguished in the form of a halo (Fig. 6A). The mafic rocks are shown as dark pixels in Fig. 6A, because of the absorption of iron minerals in the VNIR range (Gupta 2003). Salt deposits are shown with cyan color which are distinct from other units (Fig. 6A). SWIR bands are selected because nearly half or more of carbonate minerals present a distinctive absorption feature of the CO_3^{2-} ion, easily recognizable in the SWIR bands. Chlorite display spectral absorption nearby 2.32 μm, which may affect the distinguishing of carbonates (Malainine et al. 2022). Chlorite is shown in the form of green pixels in Figure 6B.

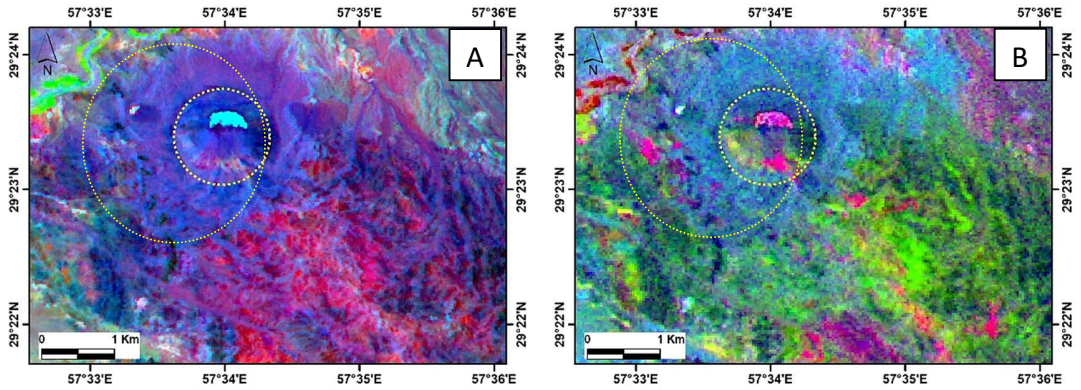

Fig.6. FCC image and decorrelation stretch technique on QHA crater rim (dashed line) and surrounding flows (dotted line): A) RGB: 631 shows Great Crater and ejected material (blue pixels), acidic and basic agglomerate and tuff (red pixels), acidic pyroclastic (purple pixels). B) RGB: 468 separates the QHA crater and ejected area, from other rock units.

The goal of different combinations of ASTER bands is to highlight certain features. This process depends upon the particular reflectance characteristics of the features involved.
In this study, the suggested band ratio from Malainine et al. (2022) were tested based on the maximum absorption in band 8 for calcite and bands 7 and 8 for dolomite (Fig. 4). The result of B5/B8, (B6+B9)/B7, (B6/B8)*(B9/B8) and (B6+B8)/B7 had little resemblance with crater area. FCC of B5/B8 (R), (B6/B7)*(B9/B8) (G), (B6+B8)/B7 (B) shows mainly pyroclastic rocks as red pixels (Fig.7A). FCC (4/1; 3/1; 12/14) had higher contrast among different geological formations based on band ratios 4/1 and 3/1 (Fig.7B). The band-ratio 12/14 enables enhancing of carbonate minerals or carbonate-bearing minerals. As a result, all rocks and sediments containing carbonate minerals, such as calcite, appear in purple or blue in the FCC image (Fig.7B).

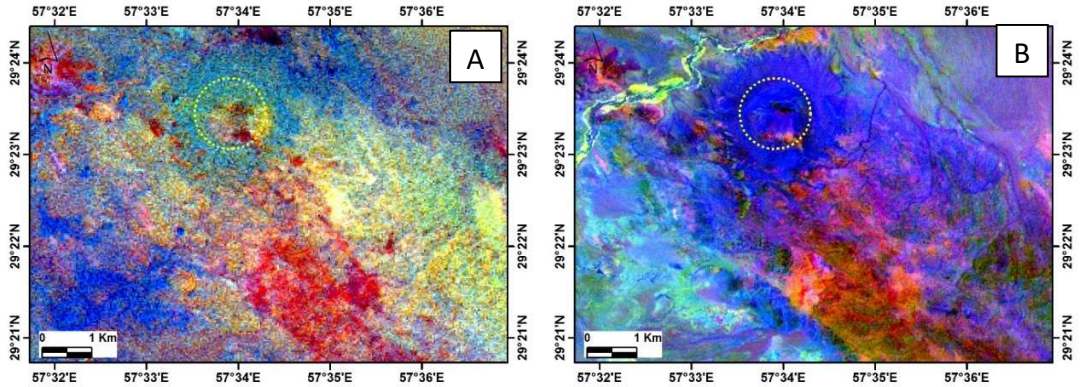

Fig.7. Image of (A) FCC of B5/B8 (R), (B6/B7)*(B9/B8) (G), (B6+B8)/B7 (B). B) FCC (B4/B1, B3/B1, B12/B14) had higher contrast among different rock units.

Analyzing and characterizing lithology using TIR ratios is also useful for identifying proper pixels to be utilized in subsequent spectral analysis. The B13/B14 band ratio image is effective to show carbonates (spectral absorption at 11.2 μm) and the (B12+B14)/B13 band ratio is suitable for showing mafic and ultramafic rocks (spectral absorption at 10.6 μm) (Rowan et al. 2006). White pixels in the TIR (B14/B12) have acceptable correspondence for mapping crater and surrounding area (Fig. 8A). Some bright pixels were also observed in the east of crater that are produced due to similarity of the spectral characteristics of the carbonate with sulfate minerals (Malainine et al. 2022). TIR bands also have been used to detect the silicate minerals (Ninomiya et al. 2005). As illustrated in Fig. 8B, the ASTER band ratio (B14+B12)/B13 is displayed in red, the band ratio B13/B14 in green, and the band ratio B14/B12 in blue channel; so, mafic and felsic rocks appear red, carbonate and pyroclastic rocks and sediment are green, silica-rich felsic rocks are blue (Fig. 8B). Although the spatial resolution of ASTER-TIR is different from SWIR and VNIR bands, it still presents a powerful tool for identifying quartz and carbonate minerals.

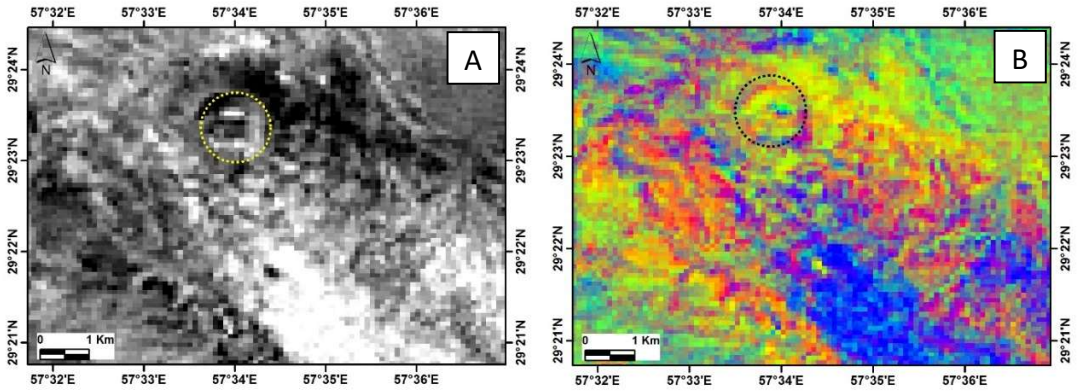

Fig.8. Band rationing of ASTER data. A) The greyscale images of B14/B12, B) Color composites from the R: (B14+B12)/B13, G: B13/B14, and B: B14/B12.

The PCA was performed on bands number 1, 2, 5 and 8 of ASTER images. The PCA eigenvectors obtained from these processes show the different contributions of each band in the resulted component (Table 2). PC2 was selected to show the crater and salt deposits based on the value and sign of its eigenvectors (Fig. 9A). PC2 displays positive eigenvector loading, in bands 1, 2 (0.587, 0.773, respectively) and negative eigenvector loading in bands 5 and 8 (-0.210 and −0.112). Thus, PC2 was chosen among the other component to enhance some representative minerals.

Table 2. Eigenvector statistics of SPCA on bands 1, 2, 5, and 8 in the QHA area.

Eigenvector	PC1	PC2	PC3	PC4
Band 1	0.137537	0.587537	0.586922	0.53982
Band 2	0.181876	0.773374	-	-0.47024
Band 5	0.684945	-	0.498589	-
Band 8	0.691993	-0.11213	-	0.499327

Band 4 ASTER located at 1.6-1.7 µm and band 6 is located in 2.185–2.225 µm region to detect the presence of some minerals, such as sulfates. Thus, the bands 1, 3, 4, and 6 were selected in PCA techniques for detecting the target area. PC2 shows negative loading for bands 3 (-0.808). Mirabilite (Na_2SO_4. $10H_2O$) displays reflection in band 3 at 0.78-0.86 µm. So, PC2 gives the target areas dark pixels. This trend is the inverse of the spectral graphs for the sulfate salt minerals (e.g., mirabilite). Hence, PC2 was inverted to highlight the selected target as bright pixels. The FCC image generated from SPCA 1346 (–PC2, PC3, PC4) is shown in figure 9B. Sulfate minerals in QHA crater are highlighted with red pixels (Fig. 9B). XRD and SEM studies on these sulfate minerals have confirmed the presence of minerals such as mirabilite (Ghaedi et al. 2016). The other PCs were utilized to enhance a variety of hydrous quartz in silicate minerals and silica-rich felsic rocks (blue pixels in Fig. 9B).

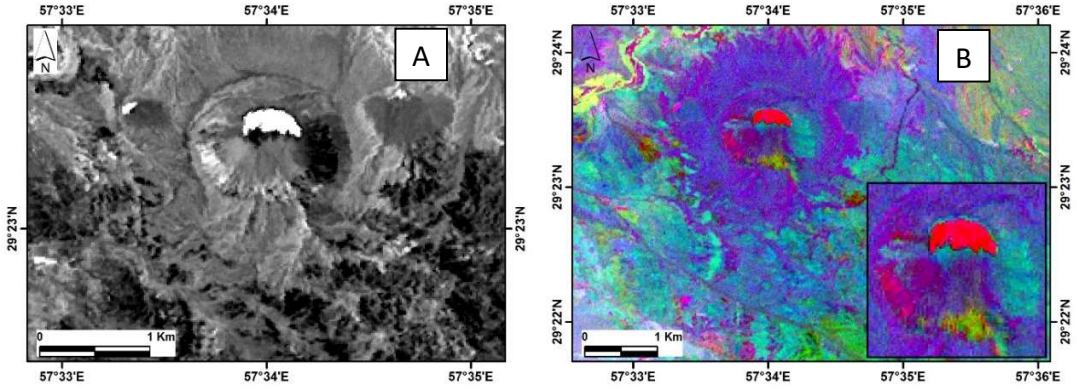

Fig.9. A) PC2 output of selected components form the SPCA on bands 1, 2, 5, and 8 (ASTER) as brighter white pixels highlighting salt in crater, and B) Color composites image generated on SPCA 1346 (–PC2, PC3, PC4) applied salt deposit in QHA crater with red pixels.

SAM classifications were applied to detect some rocks. Unlike the PCA method, the SAM has illustrated the lithological units with some degrees of false detection and result displays an acceptable matching for a limited number of rocks outcrops in the surrounding area of QHA. For example, SAM enhancing result for andesite basalt and lamprophyre, rhyolite and alkali granite is shown in figure 10. SAM technique detected this lithologies on southward of QHA, but false detection pattern is shown in alluvial units in north of QHA (Fig.10). The enhancement of tuff,

breccia and agglomerate are also associated with errors .This is probably due to the mixing of rocks with each other and the presence of various debris and rock alteration.

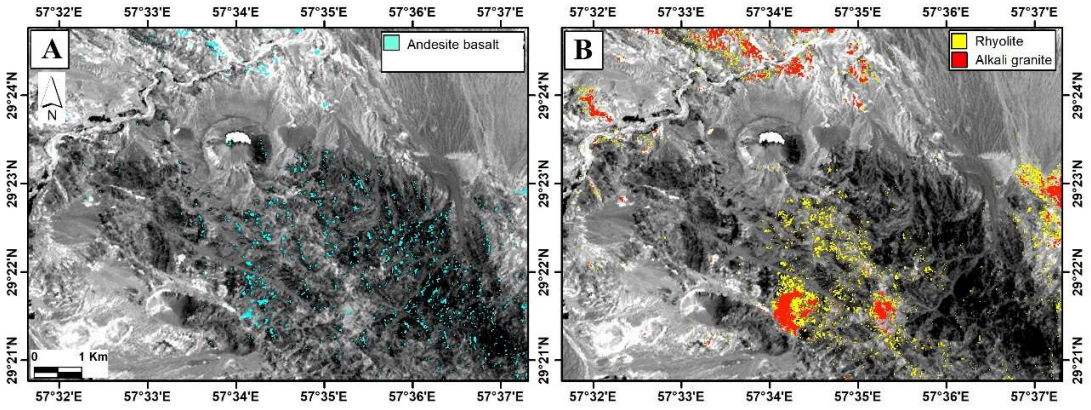

Fig. 10. SAM enhancing result for: A) andesite basalt and lamprophyre, B) Rhyolite and alkali granite.

Hydrate sulfates show a reflectance feature at ~2.4 µm that is caused by vibrations of the SO4-2 connected with H2O or OH (Cloutis et al. 2006). These spectral absorptions support the detection of certain sulfate minerals from chloride salts. Gypsum ($CaSO_4.2H_2O$) show an indicative feature at 1.45, 1.49, and 1.54, single bands near 1.75 and 1.94 µm, and a doublet at 2.22 and 2.27 µm (Bishop et al. 2014). In bassanite ($2CaSO_4.H_2O$), these bands appear as a triplet at 1.44, 1.47 and 1.54 µm, single bands at 1.78 and 1.93, and a doublet at 2.16 and 2.26 µm (Bishop et al. 2014). Mirabilite ($Na_2SO_4.10H_2O$) displays absorption index at 1.46, 1.77, 1.96 and ~2.2 µm. SAM classifications were applied to detect some specific minerals (Fig. 11). The SAM result displays an acceptable matching with some minerals in the QHA crater and surrounding area (Fig. 11). Based on SAM classification, mirabilite and gypsum are the main sulfates mineral in QHA crater (Fig. 11). Calcite, dolomite and aragonite were enhanced in the southern parts of "Great Crater" area. Aragonite is observed along the large faults such as the QHA fault. Pixels indicating chlorite and epidote are associated with andesite basaltic rocks (Fig. 11).

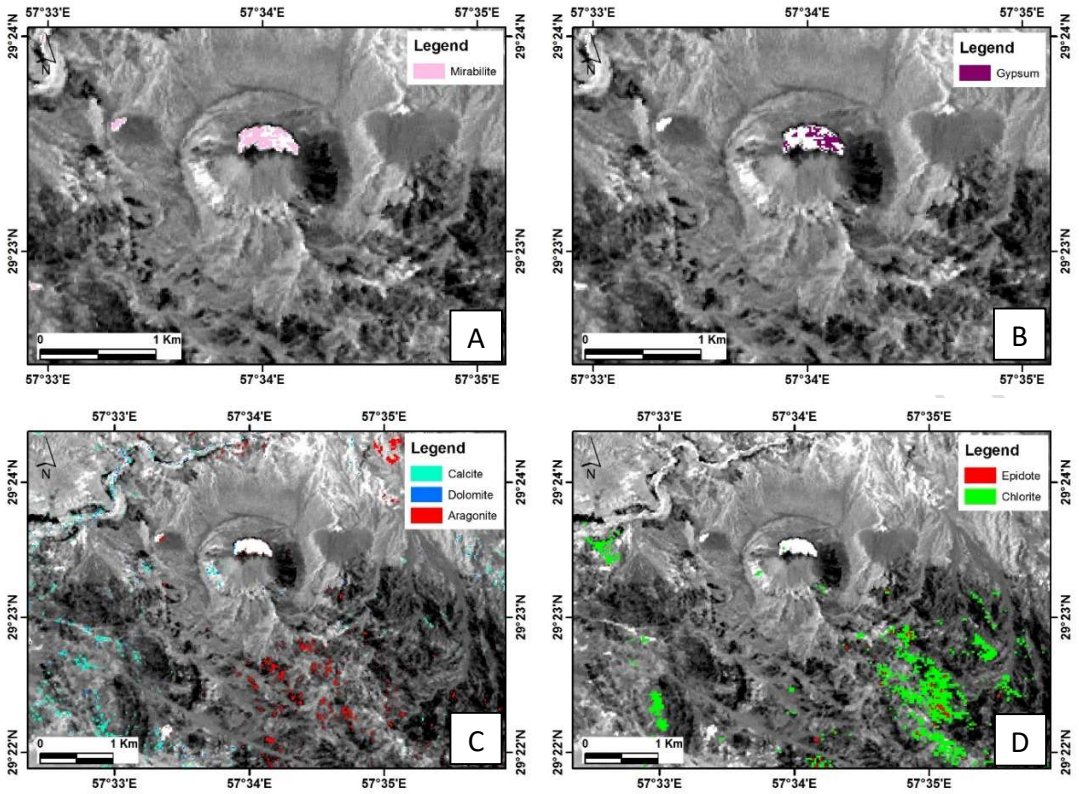

Fig. 11. SAM enhancing result for: A-D) mirabilite, gypsum, calcite, dolomite, aragonite, chlorite and epidote.

During the field studies, some areas were selected to test the detection accuracy of different rocks by remote sensing directly in the field. Ground observation of the craters shows that most parts have collapsed and some areas are left intact as detected in processing results (Fig. 12). Samples were collected from the QHA maars during field studies. These samples include tephrite, extrusive rocks, and cognate plutonic rocks, occurring as xenoliths (Fig. 12). Some magmatic calcite-bearing xenoliths in the study area show high LREE/HREE ratios having REE-rich allanite and britholite. Geochemical analyses indicate more REEs in xenoliths, some containing up to 3% modal REE-rich allanite and britholite (Table 3).

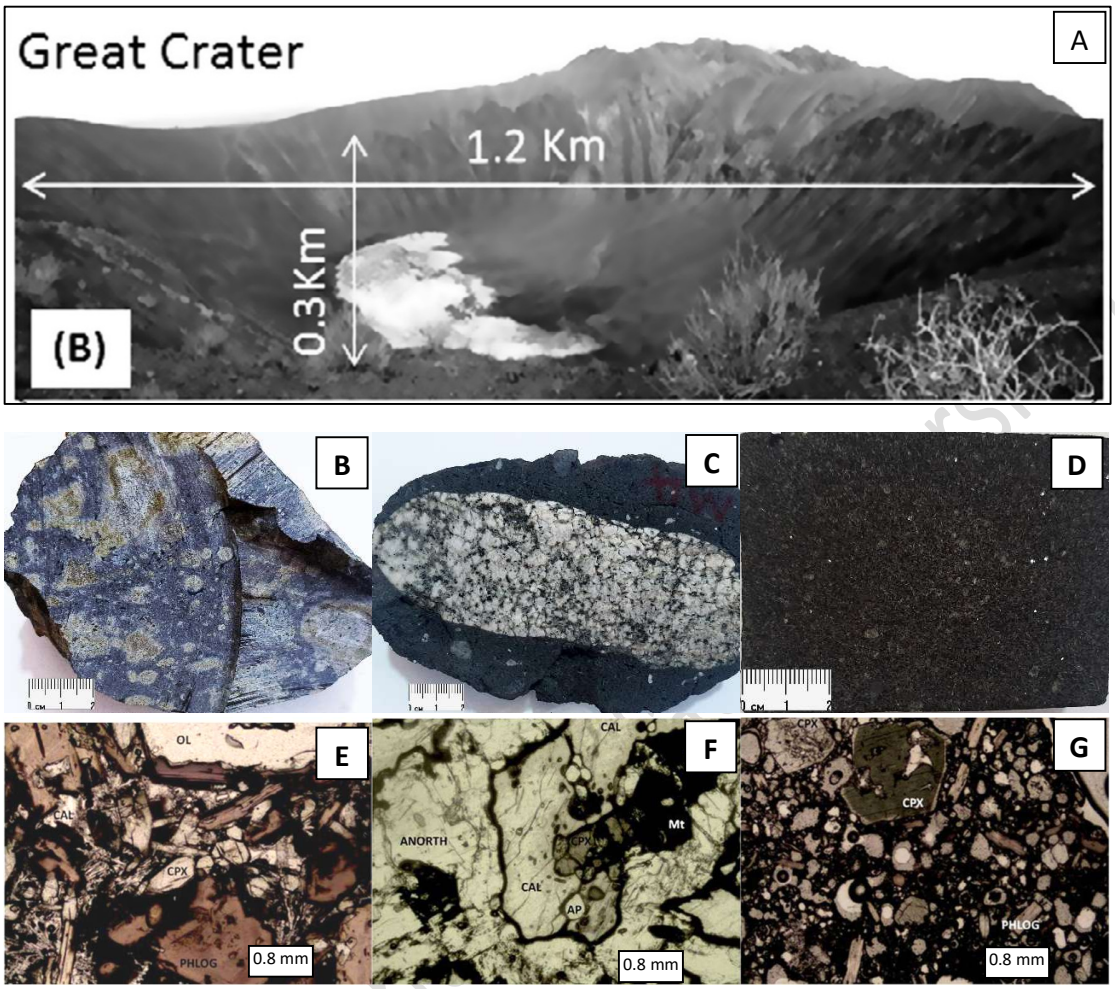

Fig. 12. A) Image of the QHA maars. B-D) Some hand samples from xenolith-bearing rocks in the study area that are observed on the inner wall of the craters: B) volcanic rocks C) plutonic rocks and D) tephrite. Photomicrograph of E) volcanic rocks (PPL), F) pyroxenite (xenolith) and calcite (CAL) as a primary igneous phase (PPL), and G) vesicular porphyritic tephrite (PPL).

Table 3. Trace element (ppm) compositions of samples from Qa'le Hasan Ali maars (Saadat et al., 2014).

Sample	M1	M-3	M-4	M-14	M-15	M-5	M-8	M-9	M-11
Ni	470	481	210	234	290	114	<20	40	<20
Cr	860	563	350	353	510	21	<20	<20	<20
V	177	181	158	183	162	192	176	224	42
Cs	3.1	3.5	6.8	8	2.6	1.4	1.3	<0.5	<0.5
Rb	199	220	145	188	167	82	58	13	66
Ba	3523	3547	2680	2847	3581	2306	1271	1423	2457
Sr	3882	2958	4008	5785	3650	5964	1990	3832	7449
Nb	17	15	23	27	23	5	8	16	129
Ta	0.9	0.9	1.5	1.7	1.1	0.4	1.5	0.6	4.7
Zr	361	224	367	379	482	112	343	245	649
Y	14	13	27	25	20	16	21	38	26
Hf	7.8	7	7.3	10	9.7	4	8	6.3	10.2
Th	13.3	8	28.9	26	27.1	5	32	19.5	156
U	2.6	2.6	11.3	13.5	6.6	1.1	7.9	3.5	73.6
Pb	26	30	123	151	74	28	34	15	85
La	92.9	90	280	233	150	116	78.5	258	826
Ce	200	199	499	426	315	281	195	617	1380
Pr	23.8	24	51.5	45	36.1	38	24.7	76.9	135
Nd	93.8	104	182	169	137	180	101	312	425
Sm	13.9	17	23.4	23	18.9	29	15.7	44.2	41.3
Eu	3.1	4.7	4.7	5.8	4.1	7	3	8.8	6.8
Gd	8.1	14.3	13.4	23	10.4	24.1	8.4	23.6	20
Tb	0.7	1.2	1.2	1.7	1	1.8	0.9	2.2	1.3
Yb	0.9	0.8	1.6	1.8	1.3	0.8	2.5	2.1	2.1
Lu	0.1	0.1	0.3	0.2	0.2	0.1	0.6	0.3	0.4

The ASTER data were applied as inputs for SVM classification. The results from the band ratio, SAM and PC performances were compared with field studies. Representative training areas were selected from known locations confirmed previously with field observation. All target classes contained a sufficient number of training samples. The training polygons contain 6431 pixels. The training data process was controlled to validate the SVM classification. The remote sensing data is not linearly separable. In this study SVM has applied with the Radial Basis Function (RBF) kernel, a non-linear kernel function. Grid search was performed as an approach to hyper-parameter (γ, C), by increasing the values of the parameters, so the γ and C were determined as 0.071 and 5, respectively. The lithological classification map of the QHA area was produced by the SVM classifier (Fig. 13A).

The RF algorithm also has been applied to characterize the lithology of unexplored neighboring area. All 14 bands of ASTER data were selected as inputs in the RF algorithm. Classification was made based on training samples (Fig. 13B). The classification of the SVM classes appears to be more acceptable due to the geology of the study area, indicating the ability of selected bands to reflect the targets.

Comparing results shows that separation of the main geological units had been obtained to an acceptable extent. Crater and its surrounding area are well classified in the SVM image. The quaternary sediment (Qt2) also is better separated in SVM. The results for andesite basalt with

pyroclastic rocks are similar in majority of the studied area; only in the southeastern part, it has a more appropriate separation in SVM, rather than RF. The silica-rich felsic units show more agreement in the RF images in the central part.

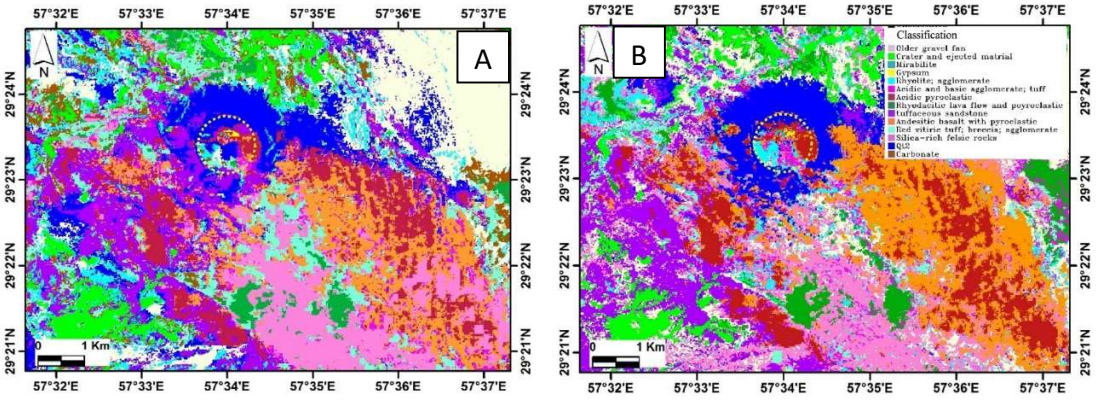

Fig. 13. Final machine learning classified map using A) SVM, B) RF.

Detailed geological map derived from ASTER data processing is presented in Figure 14. As emphasized by Shishebore (1993), the study area includes outcrops of volcanic rocks forming as basalt andesite, andesite, trachyandesite, trachyte, rhyodacite and pyroclastic rocks that are observed on the inner wall of the craters. Basalts exhibit a porphyry microlithic texture and their main minerals are plagioclase, clinopyroxene and olivine. As a result of hydrothermal fluids, mafic minerals have been transformed into chlorite, epidote and calcite. The unit that is separated as rhyodacite and pyroclastic lava in Figure 12 shows the evidence of porphyritic texture in field studies and microscopic sections. Its main minerals are quartz, alkali feldspar and plagioclase. Most of the volcanic material in the craters include tuff and volcanic breccia. Numerous dykes with a northwest-southeast trend have been injected into the pyroclastic rocks.

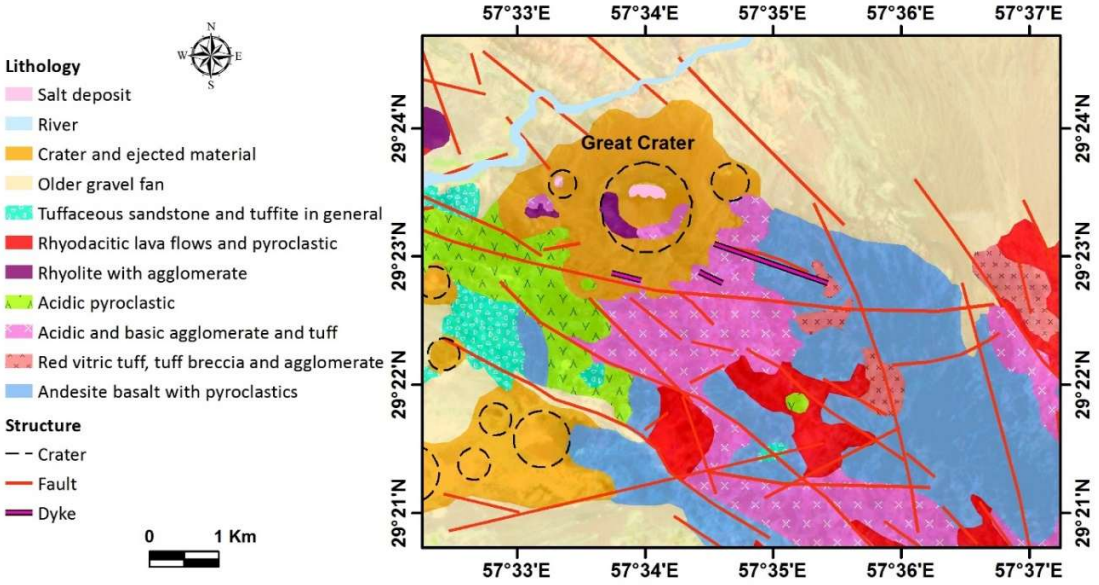

Fig. 14. Geological map of QHA area based on remote sensing results.

5. Validation and Comparative analysis

Detailed geological map derived from ASTER data processing, has been correlated and validated with field evidence, geological map scale 1:100000 (Fig. 2), and data from Saadat et al. (2014), Sabzehei (1984) and Shishebore (1993) that are consistent with available field data and geological map. Comparison of the results of the used algorithms with ground data shows PCA is an efficient technique for mapping lithology. Bands ratios with high reflectance (B4/B1, B3/B1, B12/B14), the PCA (1, 2, 5, 8) and (1, 3, 4, 6) are the most important for the study. The PC2 and PC3 show a notable match with the sulfate salt and surrendering sediments around the crater. Comparing the results show that while band ratio and principal component analysis are suitable methods for enhancing rocks such as carbonates, rhyodacite lavas and craters area, they are not appropriate for enhancing silica-rich felsic rocks (Table 4). The best-predicted were BR (B4/B1, B3/B1, B12/B14) and SPCA (1346) with 72.51%, and 70.63% overall accuracy, respectively (Table 4). Similar results of these processes indicate relative accuracy in rock unit separation. The confuse matrix and the overall accuracy (89.15%) were calculated to evaluate the performance of the SVM (Table 4). The SVM results were compared with other classified images (band ratio, and PCA). According to the result, the SVM classifier could use to map specific land cover. The Kappa statistics were applied to evaluate the result of RF classification. The confuse matrix and the overall accuracy (84%) were calculated to evaluate the performance of the RF (Table 4).

Table 4. Confusion matrix for validation dataset for some methods.

Accuracy. (%)	SVM		RF		PCA (1346)		BR (B4/B1, B3/B1, B12/B14)	
	Prod.	User.	Prod.	User.	Prod.	User.	Prod.	User.
Older gravel fan	99.14	98.71	92.18	99.72	90.78	79.20	86.98	85.44
Crater and ejected material	99.57	100	99.99	95.65	90.87	95.84	81.77	68.01
Mirabilite	85.25	83.87	91.30	100	76.92	44.78	62.30	31.67
Gypsum	67.57	80.65	91.30	100	46.15	66.67	45.95	7.11
Rhyolite, agglomerate	70.86	79.85	97.63	93.21	95.17	94.26	20.00	13.85
Acidic pyroclastic	95.42	91.03	82.93	96.23	73.43	50.19	41.01	70.54
Rhyodacitic lava flow and pyroclastic	96.10	98.67	91.47	83.69	56.02	46.72	91.25	91.13
Tuffaceous sandstone	76.25	83.39	100	92.59	76.40	81.35	60.23	79.04
Andesitic basalt with pyroclastic	82.21	79.63	96.11	91.90	76.84	70.96	63.84	74.31
Silica rich felsic rocks	98.86	94.88	91.47	83.69	21.25	5.76	38.22	31.62
Carbonate	73.33	77.19	7.48	91.67	22.48	78.84	95.49	97.76
Red vitiric tuff, breccia, agglomerate	59.84	72.33	100	97.73	100	94.80	71.16	67.22
Overall accuracy	89.15%		84.41%		70.63%		72.51%	
Kappa coefficient	0.88		0.82		0.66		0.68	

The results indicate both methods have correctly identified different lithology although there are minor differences in the target boundaries. The Kappa Statistics and the accuracy of two models are similar. The RF and SVM algorithms, compared to other methods, show an improvement in the classification of related lithologies in the study area. The outputs from these classifications were utilized to distinguish between the acidic and mafic, pyroclastic rocks and sediments. The distribution haloes of the volcanic craters are aligned with field observations. The Crater and ejected material, and silica rich felsic rocks show high producer accuracy (99.57% and 98.86%, respectively). Performance of SVM with overall accuracy of 89.15% confirms the software generated classification (Table 4).

There is a strong agreement between the rock units separated by remote sensing techniques and the field observation as well as the microscopic thin sections studied by Saadat et al. (2014). Considering these results, the maps generated here could be an effective tool for further subsurface exploration, to answer the critical research question of whether a shallow carbonatite complex with economically viable REE mineralization exists in this area.

6. Conclusion

The results of this research confirm that ASTER data and imagery are powerful tools for mapping lithology, minerals and structures of Qa'le Hasan Ali volcano in Central Iran. Various outputs derived from ASTER data define the extent of mafic and ultra-mafic and altered acidic-intermediate volcanic rocks from the QHA area. The border and types of rock units were updated based on the result of processing techniques. The Color composites from the SPCA transform technique on bands (1, 2, 5, 8) and (1, 3, 4, 6) show distribution of different rocks and minerals such as sulfate salt minerals. Salt mineralogy is distinctly different from other units. Distribution of sulfates can be easily underlined. SAM results display an acceptable fit with mirabilite, gypsum, calcite, dolomite, and aragonite minerals. Based on SAM classification, mirabilite and gypsum are

the main sulfates mineral in QHA crater. The SVM algorithm has been applied to classify the lithology. Radial basis function kernel and optimum parameters were determined as 0.071 and 5, respectively. The results show that SVM can compete with other algorithms in terms of classification accuracy. SVM with overall accuracy about 89% indicate the accuracy of classification.

Mapping the crater and salt deposit provides an overview of the REE possibility at depth. This area is also important in terms of sodium sulfate and building stones. ASTER data, along with detailed geological mapping and geochemical data of QHA crater, increase the level of confidence in the prospective area for more ground exploration in this potentially valuable locality. Therefore, it is highly recommended to conduct subsurface studies on possible REE deposits. The results presented here can be applied to exploration targets in other volcanic craters in Central Iran.

References

Abdolahadi A., Sheikhzakariaee S.J., Yazdi A., Mousavi S.Z. (2025) Plio-Quaternary Adakite Genesis and Post-collisional Processes: Whole Rock Constraints and Sr, Nd Isotopic Compositions in Alborz Magmatic Belt, Ardabil, Iran. *Journal of Mining and Environme*nt 16(2):737-765. DOI: https://doi.org/10.22044/jme.2024.14781.2801

Abrams M (2000) The Advanced Spaceborne Thermal Emission and Reflection Radiometer (ASTER): data products for the high spatial resolution imager on NASA's Terra platform, International Journal of Remote sensing 21(5):847-859. https://doi.org/10.1080/014311600210326

Abrams MJ, Brown D, Lepley L, Sadowski R (1983) Remote sensing for porphyry copper deposits in southern Arizona, Economic Geology 78:591–604. http://dx.doi.org/10.2113/gsecongeo.78.4.591

Bahrami H, Esmaeili P, Homayouni S, Pour AB, Chokmani K, Bahroudi A)2024(Machine Learning-Based Lithological Mapping from ASTER Remote-Sensing Imagery. Minerals, 14(2), p.202. https://doi.org/10.3390/min14020202

Bishop JL, Lane MD, Dyar MD, King SJ, Brown AJ, Swayze GA (2014) Spectral properties of Ca-sulfates: Gypsum, bassanite, and anhydrite, American Mineralogist 99(10):2105-2115. https://doi.org/10.2138/am-2014-4756

Boardman JW, Kruse FA (1994) Automated spectral analysis: a geological example using AVIRIS data, north Grapevine Mountains, Nevada Proceedings of the Thematic Conference on Geologic Remote Sensing, Michigan, USA, 1407-1418.

Breiman L (2017) Classification and regression trees, Routledge, 368 p. https://doi.org/10.1201/9781315139470

Clark RN (1999) Spectroscopy of rocks and minerals, and principles of spectroscopy, in: Rencz, A.N., (Ed.), Manual of Remote Sensing, Remote Sensing for the Earth Sciences 3:3-58, John Wiley and Sons, New York.

Cloutis EA, Hawthorne FC, Mertzman SA, Krenn K, Craig MA, Marcino D, Methot M, Strong J, Mustard JF, Blaney DL, Bell III JF (2006) Detection and discrimination of sulfate minerals using reflectance spectroscopy, Icarus 184(1):121-157. http://dx.doi.org/10.1016/j.icarus.2006.04.003

Crosta AP, De Souza Filho CR, Azevedo F, Brodie C (2003) Targeting key alteration minerals in epithermal deposits in Patagonia, Argentina, using ASTER imagery and principal component analysis, International Journal of Remote Sensing 24(21):4233–4240. http://dx.doi.org/10.1080/0143116031000152291

Dabiri R., Mollai H., Yazdi A., Ghaffari M. (2019) Investigation of mineral chemistry, thermobarometry and fuzzy equilibrium of the basic Plio-Quaternary volcanic rocks in NE Varzeghan. *Quaternary Journal of Iran* 4 (4): 377-394.

Dennison PE, Halligan KQ, Roberts DA (2004) A comparison of error metrics and constraints for multiple endmember spectral mixture analysis and spectral angle mapper, Remote Sensing of Environment 93(3):359–367. https://doi.org/10.1016/j.rse.2004.07.013

Djokovic´I, Dimitrijevic´MN, Cvetic´ S, Dimitrijevic´ MD (1972), "Geological map of Khaneh Khatun, scale 1:100000 (sheet 7548), Geological survey of Iran.

Farhadi S, Afzal P, Boveiri Konari M, Daneshvar Saein L, Sadeghi B (2022) Combination of Machine Learning Algorithms with Concentration-Area Fractal Method for Soil Geochemical Anomaly Detection in Sediment-Hosted Irankuh Pb-Zn Deposit, Central Iran, Minerals 12 (6):689. https://doi.org/10.3390/min12060689

Farhadi S, Tatullo S, Boveiri Konari M, Afzal P (2024) Evaluating StackingC and ensemble models for enhanced lithological classification in geological mapping. Journal of Geochemical Exploration 260, 107441. https://doi.org/10.1016/j.gexplo.2024.107441

Fujisada H)1995 (Design and Performance of ASTER Instrument, Proceedings of the International Society for Optical Engineering, 2583:16–25.

Gaffey SJ (1986) Spectral reflectance of carbonate minerals in the visible and near infrared (0.35-2.55 microns); calcite, aragonite, and dolomite, American Mineralogist 71(1-2):151-162. https://doi.org/10.1029/JB092iB02p01429

Ghaedi A, Moradian A, Ahmadipour H (2016) Geochemical studies on evaporitic minerals, with the emphasis on sodium sulfate, in Tutak craters of Rayen Town (Kerman Province), Iranian Journal of Crystallography and Mineralogy 24(1):179-188. http://ijcm.ir/article-1-126-fa.html

Ghasempour M.R., Ghazi J.M., Biabangard H., Dabiri R. (2014) Petrogenic significance of the Plio-Quaternary Nehbandan mafic lavas, Eastern Iran. *Iranian Journal of Earth Sciences* 6(2):133-141.

Gojkovic´ SE (1972) Qal'eh Hasan Ali impact craters area, south-central Iran, Geological Survey of Iran, Iran, Tehran, Internal Report.

Gupta RP (2003) Remote Sensing Geology, 2nd ed. Berlin, Germany: Springer, 655 p. http://dx.doi.org/10.1007/978-3-662-05283-9

Hadigheh SMH, Ranjbar H (2013) Lithological mapping in the eastern part of the central Iranian volcanic belt using combined ASTER and IRS data, Journal of the Indian Society of Remote Sensing 41:921-931. https://doi.org/10.1007/s12524-013-0284-1

Hunt GR (1977) Spectral signatures of particulate minerals in the visible and near infrared, Geophysics 42(3):501–513. https://doi.org/10.1190/1.1440721

Kavak KS (2005) Recognition of gypsum geohorizons in the Sivas Basin (Turkey) using ASTER and Landsat ETM+ images, International Journal of Remote Sensing, 26, 4583 - 4596. https://doi.org/10.1080/01431160500185607

Kruse FA, Lefkoff AB, Boardman JW, Heidebrecht KB, Shapiro AT, Barloon PJ, Goetz AFH (1993) The spectral image processing system (SIPS)-interactive visualization and analysis of imaging spectrometer data, Remote Sensing of Environment 44(2-3):145-163. https://doi.org/10.1016/0034-4257(93)90013-N

Laukamp C, Rodger A, LeGras M, Lampinen H, Lau IC, Pejcic B, Stromberg J, Francis N, Ramanaidou E (2021) Mineral Physicochemistry Underlying Feature-Based Extraction of Mineral Abundance and Composition from Shortwave, Mid and Thermal Infrared Reflectance Spectra, Minerals 11 (4):347. https://doi.org/10.3390/min11040347

Libeesh NK, Naseer KA, Arivazhagan S, Abd El-Rehim AF, ALMisned G, Tekin HO (2022) Characterization of Ultramafic–Alkaline–Carbonatite complex for radiation shielding competencies: An experimental and Monte Carlo study with lithological mapping, Ore Geology Reviews 142:104735. http://dx.doi.org/10.1016/j.oregeorev.2022.104735

Mahvash Mohammadi N, Hezarkhani A)2020(A comparative study of SVM and RF methods for classification of alteration zones using remotely sensed data. Journal of Mining and Environment, 11(1):49-61. https://doi.org/10.22044/jme.2019.7956.1664

Malainine CE, Raji O, Ouabid M, Khouakhi A, Bodinier JL, Laamrani A, El Messbahi H, Youbi N, Boumehdi MA (2022) An integrated ASTER-based approach for mapping carbonatite and iron oxide-apatite deposits, Geocarto International 37(22):6579-6601. https://doi.org/10.1080/10106049.2021.1953617

Mars JC, Rowan LC (2011) ASTER spectral analysis and lithologic mapping of the Khanneshin carbonatite volcano, Afghanistan, Geosphere 7(1):276–289. http://dx.doi.org/10.1130/GES00630.1

Masoumi F, Eslamkish T, Abkar AA, Honarmand M and Harris JR)2017(Integration of spectral, thermal, and textural features of ASTER data using Random Forests classification for lithological

mapping. Journal of African Earth Sciences, 129:445-457. https://doi.org/10.1016/j.jafrearsci.2017.01.028

Milton DJ (1976) Qal'eh Hassan Ali Maars, Central Iran, Bulletin of Volcanology 40(3):201–208. https://doi.org/10.1007/BF02597000

Mollai H., Dabiri R., Torshizian H.A., Pe-Piper G., Wang W.E. (2021) Upper Neoproterozoic garnet-bearing granites in the Zeber-Kuh region from east central Iran micro plate: Implications for the magmatic evolution in the northern margin of Gondwanaland. *Geologica Carpathica* 72 (6): 461-81. DOI: http://dx.doi.org/10.31577/GeolCarp.72.6.2

Mundt JT, Streutker DR, Glenn NF (2007) Partial Unmixing of Hyperspectral Imagery: Theory and methods, ASPRS Annual Conference Tampa, Florida, USA, 1-12.

Nabilou M, Afzal P, Arian M, Adib A, Kazemi Mehrnia A, Jami M, Kheyrollahi H, Akhavan Aghdam, MR, Ameri A, Daneshvar Saein L (2022) Determination of relationship between Rare Earth Elements (REEs) mineralization and major faults using fractal modeling in Gazestan deposit, central Iran, Bollettino di Geofisica Teorica ed Applicata 63 (3):495-518. https://doi.org/10.4430/bgo00388

Nazari M., Arian M.A., Solgi A., Zareisahamieh R., Yazdi A. (2023) Geochemistry and tectonomagmatic environment of Eocene volcanic rocks in the Southeastern region of Abhar, NW Iran. *Iranian Journal of Earth Sciences* 15(4): 228-247. DOI: https://doi.org/10.30495/ijes.2023.1956689.1746

Ninomiya Y, Fu B, Cudahy TJ (2005) Detecting lithology with Advanced Spaceborne Thermal Emission and Reflection Radiometer (ASTER) multispectral thermal infrared "radiance-at-sensor" data, Remote Sensing of Environment 99(1-2):127-139. https://doi.org/10.1016/j.rse.2005.06.009

Ousta S.h., Ashja-Ardalan A., Yazdi A., Dabiri R., Arian M.A. (2024) Petrogenesis and tectonic implications of Miocene dikes in the southeast of Bam (SE Iran): Constraints on the development of active continental margin. *Geopersia* 14 (1): 89-111. DOI: https://doi.org/10.22059/geope.2023.364334.648729

Pal M, Mather PM (2005) Support vector machines for classification in remote sensing, International Journal of Remote Sensing 26:1007–1011. https://doi.org/10.1080/01431160512331314083

Pang KN, Chung SL, Zarrinkoub MH, Wang F, Kamenetsky VS, Lee HY (2015) Quaternary High-Mg ultrapotassic rocks from the Qal'eh Hasan Ali maars, southeastern Iran: petrogenesis and geodynamic implications, Contributions to Mineralogy and Petrology 170(3):1-19. http://dx.doi.org/10.1007/s00410-015-1183-y

Pirajno F (2015) Intracontinental anorogenic alkaline magmatism and carbonatites, associated mineral systems and the mantle plume connection, Gondwana Research 27(3):1181-1216. https://doi.org/10.1016/j.gr.2014.09.008

Rahmani N, Sekandari M, Pour AB, Ranjbar H, Carranza EJM (2025) Evaluation of support vector machine classifiers for lithological mapping using PRISMA hyperspectral remote sensing data: Sahand–Bazman magmatic arc, Central Iran, Remote Sensing Applications: Society and Environment, p.101449. https://doi.org/10.1016/j.rsase.2025.101449

Rajendran S, Nasir S (2013) ASTER spectral analysis of ultramafic lamprophyres (carbonatites and aillikites) within the Batain Nappe, northeastern margin of Oman: a proposal developed for spectral absorption, International Journal of Remote Sensing 34(8):2763–2795. http://dx.doi.org/10.1080/01431161.2012.748941

Ramsey MS, Flynn IT (2020) The Spatial and Spectral Resolution of ASTER Infrared Image Data: A Paradigm Shift in Volcanological Remote Sensing, Remote Sensing 12(4):738. https://doi.org/10.3390/rs12040738

Rowan LC, Mars JC, Simpson CJ (2006) Lithologic mapping of the Mordor, Northern Territory, Australia ultramafic complex using Advanced Spaceborne Thermal and Reflection Radiometer (ASTER) data, Remote Sensing of Environment 99(1-2):105–126. https://doi.org/10.1016/j.rse.2004.11.021

Saadat S, Stern CR (2011) Petrochemistry and genesis of olivine basalts from small monogenetic parasitic cones of Bazman stratovolcano, Makran arc, southeastern Iran, Lithos 125(1–2):607-619. https://doi.org/10.1016/j.lithos.2011.03.014

Saadat S, Stern CR, Moradian A (2014) Petrochemistry of ultrapotassic tephrites and associated cognate plutonic xenoliths with carbonatite affinities from the late Quaternary Qa'le Hasan Ali maars, central Iran, Journal of Asian Earth Sciences 89:108-122. https://doi.org/10.1016/j.jseaes.2014.03.021

Sabzehei M (1984) Petrogenesis and origin of late Quaternary alkaline–carbonatite magmatic activities in the Qa'le Hasan Ali Rayen area, Geological Survey of Iran, Iran, Tehran, internal Report, 143 p.

Salehpour S., Arian M.A., Rad A.J., Zarei Sahamieh R., Yazdi A. (2025) Geochemistry and technomagmatic environment of Eocene volcanic rocks in Yuzbashi Chay region, west of Qazvin (Iran). *Iranian Journal of Earth Sciences* 17(1): 1-13. DOI: https://doi.org/10.57647/j.ijes.2025.1701.04

Shishebore F (1993) Petrography, geochemistry and petrology investigation from Rayen Qa'le Hasan Ali lamproites rocks, M.Sc. Thesis, Dept. Earth sciences, Shahid Bahonar University, Kerman, Iran.

Van der Meer FD (1995) Spectral reflectance of carbonate mineral mixtures and bidirectional reflectance theory: Quantitative analysis techniques for application in remote sensing, Remote Sensing Reviews 13(1-2):67–94. https://doi.org/10.1080/02757259509532297

Accepted manuscript (author version)

Yazdi A., Ashja-Ardalan A., Emami M.H., Dabiri R., Foudazi M. (2019) Magmatic interactions as recorded in plagioclase phenocrysts of quaternary volcanics in SE Bam (SE Iran). *Iranian Journal of Earth Sciences* 11(3): 215-224. DOI: https://doi.org/10.30495/ijes.2019.667379